

# Air-sea interactions and water mass transformation during a katabatic storm in the Irminger Sea

Oliver Gutjahr<sup>1</sup>, Johann H Jungclaus<sup>2</sup>, Nils Brüggemann<sup>3</sup>, Helmuth Haak<sup>4</sup>, and Jochem Marotzke<sup>2</sup>

<sup>1</sup>Universität Hamburg

<sup>2</sup>Max Planck Institute for Meteorology

<sup>3</sup>University of Hamburg

<sup>4</sup>Max-Planck-Institut fuer Meteorologie

November 23, 2022

## Abstract

We use a global 5-km resolution model to analyse the air-sea interactions during a katabatic storm in the Irminger Sea originating from the Ammassalik valleys. Katabatic storms have not yet been resolved in global climate models, raising the question of whether and how they modify water masses in the Irminger Sea. Our results show that dense water forms along the boundary current and on the shelf during the katabatic storm due to the heat loss caused by the high wind speeds and the strong temperature contrast. The dense water contributes to the North Atlantic Deep Water and thus to the Atlantic Meridional Overturning Circulation (AMOC). The katabatic storm triggers a polar low, which in turn amplifies the near-surface wind speed in a positive feedback, in addition to acceleration from a breaking mountain wave. Resolving katabatic storms in global models is therefore important for the formation of dense water in the Irminger Sea, which is relevant to the AMOC, and for the large-scale atmospheric circulation by triggering polar lows.

1           **Air-sea interactions and water mass transformation**  
2           **during a katabatic storm in the Irminger Sea**

3           **O. Gutjahr<sup>1,2</sup>, J. H. Jungclaus<sup>2</sup>, N. Brüggemann<sup>1,2</sup>, H. Haak<sup>2</sup>, J. Marotzke<sup>2,3</sup>**

4                           <sup>1</sup>Institut für Meereskunde, Universität Hamburg, Hamburg, Germany.

5                           <sup>2</sup>Max Planck Institute for Meteorology, The Ocean in the Earth System, Hamburg, Germany.

6                           <sup>3</sup>Center for Earth System Research and Sustainability (CEN), Universität Hamburg, Germany.

7           **Key Points:**

- 8           • For the first time, the direct effect of a katabatic storm on the ocean has been sim-  
9           ulated in a global climate model
- 10          • The katabatic storm triggers a polar low and develops in positive feedback with  
11          it
- 12          • Katabatic storms induce water mass transformation over the shelf and boundary  
13          current that contributes to the North Atlantic Deep Water

---

Corresponding author: O. Gutjahr, [oliver.gutjahr@mpimet.mpg.de](mailto:oliver.gutjahr@mpimet.mpg.de)

**Abstract**

We use a global 5-km resolution model to analyse the air-sea interactions during a katabatic storm in the Irminger Sea originating from the Ammassalik valleys. Katabatic storms have not yet been resolved in global climate models, raising the question of whether and how they modify water masses in the Irminger Sea. Our results show that dense water forms along the boundary current and on the shelf during the katabatic storm due to the heat loss caused by the high wind speeds and the strong temperature contrast. The dense water contributes to the North Atlantic Deep Water and thus to the Atlantic Meridional Overturning Circulation (AMOC). The katabatic storm triggers a polar low, which in turn amplifies the near-surface wind speed in a positive feedback, in addition to acceleration from a breaking mountain wave. Resolving katabatic storms in global models is therefore important for the formation of dense water in the Irminger Sea, which is relevant to the AMOC, and for the large-scale atmospheric circulation by triggering polar lows.

**Plain Language Summary**

Katabatic storms originating from the Ammassalik area in southeast Greenland have so far not been resolved in global climate models because their spatial extent is smaller than typical grid resolutions. We analyse a case study of an katabatic storm from a novel storm-resolving (5 km) simulation with the globally coupled ICON-ESM and demonstrate that this katabatic storm causes substantial heat loss in the Irminger Sea's boundary current, leading to dense water formation and sinking on the southeast Greenland shelf. These results suggest that resolving such katabatic storms in global models could affect the location and intensity of the sinking of the global conveyor belt in the subpolar North Atlantic.

**1 Introduction**

Recent observations made with the Overturning in the Subpolar North Atlantic Program (OSNAP) array allowed for the first time to directly relate deep water mass formation in the subpolar North Atlantic and overturning variability. These data indicate that water mass transformation east of Greenland is largely responsible for the overturning of the Atlantic Meridional Overturning Circulation (AMOC) and its variability (Lozier et al., 2019). However, the exact role of the Irminger and Labrador Sea in AMOC variability is still controversial. In particular, it is discussed whether deep water formation in the Labrador Sea contributes only marginally to AMOC variability (Desbruyères et al., 2019; Menary et al., 2020), whether there has been a shift in deep water formation from the Labrador to the Irminger Sea over the past decade (Rühs et al., 2021) or whether deep water formation in the Labrador Sea dominates multidecadal AMOC variability, while that in the Irminger Sea influences high-frequency variability (Yeager et al., 2021).

In the Irminger Sea, strong surface heat and momentum fluxes were found to be most important for generating density anomalies in the boundary currents, such as the East Greenland-Irminger Current (EGIC) or over the Reykjanes Ridge (LeBras et al., 2020; Petit et al., 2020). Based on OSNAP, an upper Irminger Sea Intermediate Water (uSIW;  $\sigma_\theta = 27.65$  to  $27.73 \text{ kg m}^{-3}$ ) has been identified forming at the edge of the EGIC (LeBras et al., 2020). This intermediate water contributes to deep water formation alongside the denser water masses formed by deep convection in the basin interior (Bacon et al., 2003; Pickart et al., 2003; de Jong et al., 2012, 2018) and overflows from the Nordic Seas (Chafik & Rossby, 2019). The dense water anomalies from the boundary current are transported southward into the Labrador Sea where they correlate strongly with AMOC variability (Desbruyères et al., 2019; Petit et al., 2020; Menary et al., 2020).

63 However, the surface fluxes producing these density anomalies are likely underes-  
 64 timated in current global climate models, such as those involved in CMIP6 (Eyring et  
 65 al., 2016) or in CMIP6 HighResMIP (Haarsma et al., 2016), because the wind systems  
 66 that cause these strong fluxes are mesoscale and therefore not or insufficiently resolved.  
 67 In particular, katabatic winds and storms originating from the Greenland Ice Sheet cause  
 68 a strong loss of heat and buoyancy of the shelf water and EGIC due to the high wind  
 69 speeds and the cold and dry air they carry over the relatively warm ocean. They con-  
 70 tribute to about one fifth of the total winter heat loss (Oltmanns et al., 2014). Resolv-  
 71 ing katabatic storms could therefore affect the deep water formation in the Irminger Sea  
 72 and hence its role for AMOC variability.

73 Katabatic winds are density-driven currents originating from large ice sheets, such  
 74 as in Greenland, due to radiative cooling of the surface boundary layer. They dominate  
 75 the near-surface wind field and their velocity is highest near the ice sheet margins. The  
 76 strongest downslope katabatic winds occur frequently in the Ammassalik area on the south-  
 77 east coast of Greenland, where the katabatic flow converges in the narrow fjords and ac-  
 78 celerates because of the steep topography (Heinemann & Klein, 2002). This gravitational  
 79 acceleration becomes stronger the colder and thus denser the air is. When a synoptic cy-  
 80 clone is located over the Irminger Sea, the overlying geostrophic flow can strengthen the  
 81 pure katabatic flow to gale force, sometimes even hurricane force, which then causes se-  
 82 vere destruction (Rasmussen, 1989; Oltmanns et al., 2014). Often these two mechanisms  
 83 work together to form a katabatic storm. However, a third mechanism is the breaking  
 84 of mountain or lee waves over the steep slopes of southeast Greenland (Oltmanns et al.,  
 85 2015), which transfer momentum into the boundary layer and further accelerate the kata-  
 86 batic flow. These hazardous katabatic storms or "piteraqs" (Greenlandic) are a regular  
 87 phenomena and the most severe on record was hitting the community of Tasilaq (Am-  
 88 massalik) in February 1970 with a peak velocity of nearly  $90 \text{ m s}^{-1}$ .

89 Over the Irminger Sea, katabatic winds from Ammassalik can trigger mesocyclones  
 90 (Klein & Heinemann, 2002), also called polar lows (Kolstad, 2011; Moreno-Ibáñez et al.,  
 91 2021). Polar lows frequently form over the Irminger Sea (Bracegirdle & Gray, 2008; Zahn  
 92 & von Storch, 2008; Kolstad, 2011; Stoll et al., 2018), which is related to cyclogenesis in  
 93 the lee of Greenland's high orography (Blechschmidt et al., 2009; Kristjánsson et al., 2011)  
 94 and with marine cold air outbreaks (MCAO, Kolstad et al., 2009), including katabatic  
 95 winds (Klein & Heinemann, 2002). In particular, two mechanisms are at work (Klein &  
 96 Heinemann, 2002). First, the convergence of the katabatic flow in the valleys lead to vor-  
 97 tex stretching that enhances cyclonic vorticity that is transported eastward by the hor-  
 98 izontal flow. Second, advection of cold air from the Greenland ice sheet over the rela-  
 99 tively warm Irminger Sea leads to high sensible and latent heat fluxes, whose divergences  
 100 reduce the atmospheric stratification. If clouds form over the Irminger Sea because of  
 101 the large latent heat fluxes, atmospheric stratification is further reduced due to release  
 102 of latent heat. Katabatic winds from Ammassalik therefore increase low-level baroclin-  
 103 icity that favours the formation of polar lows.

104 On average, about 5 to 11 polar lows form in the Irminger Sea per winter, depend-  
 105 ing on the detecting method and data set analysed (Zahn & von Storch, 2008; Kolstad,  
 106 2011), while katabatic storms in the Ammassalik area occur about seven times per year,  
 107 reaching about  $20 \text{ m s}^{-1}$  (Oltmanns et al., 2014). If sea ice is present, katabatic winds  
 108 from the Ammassalik valleys can open coastal polynyas (Heinemann, 2003). The brine  
 109 released during the formation of new sea ice then contributes to even denser shelf wa-  
 110 ters. Katabatic winds may also be important for fluxing fresh shelf water of Arctic ori-  
 111 gin into the interior basin of the Irminger Sea, thereby affecting the stratification. How  
 112 exactly freshwater is transported off-shelf is still unclear, but wind is thought to be the  
 113 main driver (Duyck & de Jong, 2021).

114 Resolving katabatic storms and small-scale orographic features in GCMs is there-  
 115 fore crucial for the cooling and densification of the EGIC, but also for the feedback of

116 small-scale processes to the synoptic scale in terms of polar low formation and exchange  
 117 of momentum and energy. Because of the teleconnectivity that the Irminger Sea exerts  
 118 on the AMOC and the large-scale atmospheric circulation, a global coupled model is needed  
 119 to capture these interactions. However, the atmospheric resolution of CMIP6 models is  
 120 on the order of 50 to 100 km, with some exceptions of 25 km for individual HighResMIP  
 121 models. Katabatic winds and other mesoscale wind systems around Greenland, such as  
 122 tip jets, require model resolutions of less than 10 to 15 km to be adequately represented  
 123 (DuVivier & Cassano, 2013; Oltmanns et al., 2015; Gutjahr & Heinemann, 2018). A res-  
 124 olution of 5 km is even better to capture the channelling effects in the narrow fjords and  
 125 the momentum transfer by breaking mountain waves over the steep coastal slopes (Oltmanns  
 126 et al., 2015). Katabatic winds further require a high vertical resolution in the surface bound-  
 127 ary layer where also low-level jets form (Heinemann, 2003). In addition, a non-hydrostatic  
 128 dynamical core is needed to simulate the strong vertical velocities during a katabatic storm,  
 129 especially where mountain waves breaks causing a katabatic jump and generating grav-  
 130 ity waves.

131 Since a high resolution is required, katabatic storms have so far only been studied  
 132 with regional atmosphere models (e.g. Oltmanns et al., 2014, 2015). Even though high  
 133 model resolution can be achieved in regional models, they have two severe limitations.  
 134 First, they were used as stand-alone, i.e. they were not coupled to an ocean model, thereby  
 135 neglecting air-sea interactions with the ocean, including changes to the circulation and  
 136 the water mass characteristics. Second, because of their limited domain they do not al-  
 137 low for feeding back the effects of the small scales to the large scales, thereby neglect-  
 138 ing teleconnections. Although the interactions across scales is sometimes realized in re-  
 139 gional models by so-called two-way nesting, the problem remains that the rest of the globe  
 140 is not affected by the resolved small scales within the domain. Similar arguments apply  
 141 to studies with ocean stand-alone simulations, which must be driven by atmospheric data  
 142 that cannot respond to feedbacks with the ocean and are often too coarse to represent  
 143 the mesoscale winds around Greenland (e.g. Paquin et al. (2016)).

144 Since the resolution of global climate models has so far been too coarse to resolve  
 145 katabatic storms (Mc Innes et al., 2011), their influence on the EGIC was likely under-  
 146 estimated. Although there were attempts to account for their effects on the ocean cir-  
 147 culation (Condron et al., 2008), such parameterizations were never widely used in global  
 148 models. Here we analyze for the first time a katabatic storm or piteraq that triggers a  
 149 polar low, interacts with it and causes water mass transformation in the Sermilik Trough  
 150 (ST) and EGIC. We exploit a frontier simulation with the globally coupled, storm- and  
 151 eddy-resolving (5 km) ICON-ESM, which is almost two years long. An overview of the  
 152 simulation will be presented elsewhere.

153 The analyzed katabatic storm is the most intense in simulation, which is why we  
 154 chose it for our case study. Even though the simulation is too short to link density anom-  
 155 alies in the boundary current to the AMOC, the model is potentially able to simulate this  
 156 linkage.

157 The remainder of the manuscript is organized as follows: in section 2 we describe  
 158 the model configuration, section 3 outlines the development of the katabatic storm, in  
 159 section 4 and 5 the analyses of the air-sea interactions and induced response of the ocean  
 160 are presented. We conclude in section 6.

## 161 2 Model configuration

162 We analyze the development of a katabatic storm in the Irminger Sea and its in-  
 163 duced air-sea fluxes and water mass transformation in a frontier simulation made with  
 164 ICON-ESM (ICOsahedral Non-hydrostatic - Earth System Model; Zängl et al. (2015);  
 165 Korn (2017); Giorgetta et al. (2018); Jungclaus et al. (2021)), which is participating in

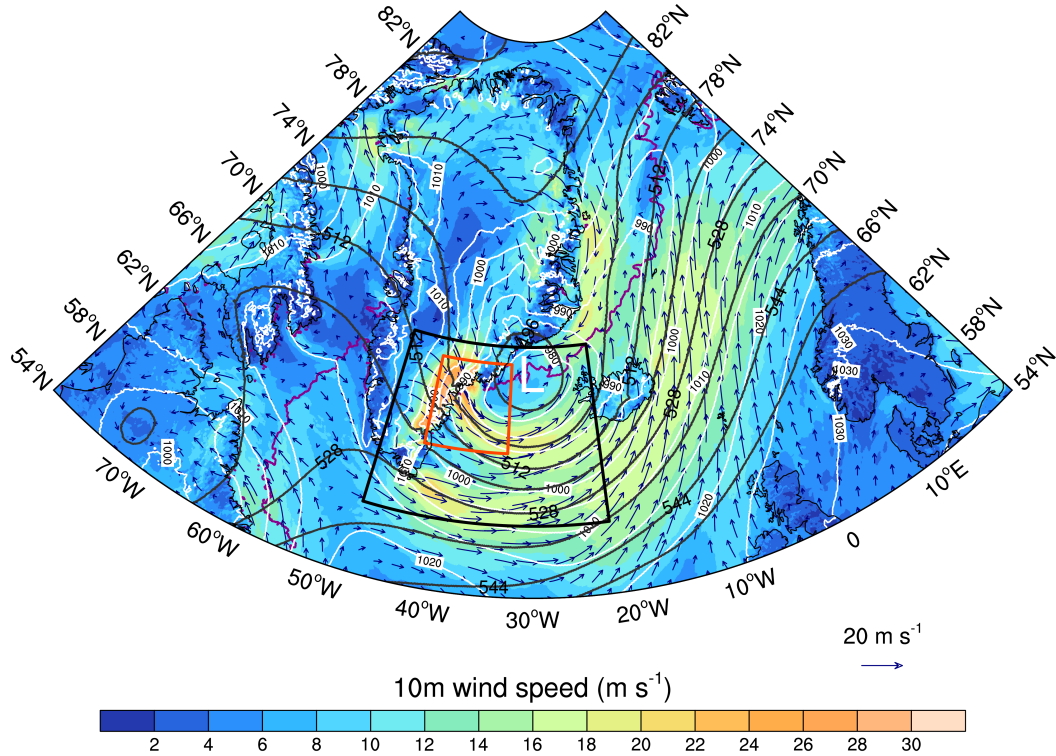


**Figure 1.** Synoptic situation on simulation day for 29 February 2020 in ICON-ESM. Shown is the daily mean of 10 m wind speed (colour shaded) and the wind vectors. Overlain is the daily mean sea-level pressure in hPa (white contours), the geopotential height at 500 hPa in gpm (dark grey contours), and the 15% sea ice concentration (magenta contour). The reference scale of the wind vectors is given at the bottom right. The "L" symbol marks the centre of the polar low that is moving towards Denmark Strait. The black box marks the area of the Irminger Sea and the orange box the Ammassalik area.

166 the second phase of the DYnamics of the Atmospheric general circulation On Non-hydrostatic  
 167 Domains (DYAMOND) Winter initiative (Stevens et al., 2019, and [https://www.esiwave](https://www.esiwave.eu/services/dyiamond/winter)  
 168 [.eu/services/dyiamond/winter](https://www.esiwave.eu/services/dyiamond/winter)). The model is globally coupled and was run at a hor-  
 169 izontal resolution of 5 km, both in the non-hydrostatic atmospheric component (ICON-  
 170 A) and in the hydrostatic ocean/sea ice component (ICON-O). The grid resolution is thereby  
 171 defined as the square root of the cell area of the spherical triangles (Zängl et al., 2015).  
 172 Both components use a high vertical resolution. ICON-A is run with 90 terrain-following,  
 173 hybrid sigma levels, with the top layer at 75 km height, which corresponds to the oper-  
 174 ational weather forecast configuration at Deutscher Wetterdienst (DWD). Thirteen lev-  
 175 els are distributed within the lower 2000 m over the Irminger Sea and 20 levels over land  
 176 in the Ammassalik area. ICON-O uses 128 z-levels without a partial bottom cell param-  
 177 eterization. Ninety-six levels are distributed within the upper 500 m.

178 A main purpose of the DYAMOND (Winter) initiative is to run atmosphere mod-  
 179 els at a convection and storm resolving resolution ( $\leq 5$  km) and the ocean models at a  
 180 similar resolution. The vertical resolution must be at least 75 levels in both spheres in  
 181 order to study the mesoscale ocean-atmosphere coupling. Although the model resolu-  
 182 tion approaches the km scale, the smallest scale that is fully resolved in the model - the  
 183 effective resolution - is much larger than the grid spacing or nominal model resolution.  
 184 The effective resolution is usually determined by comparing modeled and observed ki-

netic energy spectra (Skamarock, 2004). For ICON-A, the effective resolution is about 7 times the mesh size (Zängl et al., 2015; Neumann et al., 2019), which corresponds to 35 km for our configuration. Below this scale, kinetic energy is dissipated due to physical parameterizations, orographic smoothing, numerical diffusion and aliasing effects (Neumann et al., 2019; Klaver et al., 2020). Therefore, small-scale atmospheric processes, such as convection or orographic drag, are still partially unresolved in this model configuration. However, studies with regional models have shown that a nominal model resolution of less than 10 to 15 km is sufficient to resolve the main features of mesoscale wind systems around Greenland (DuVivier & Cassano, 2013; Gutjahr & Heinemann, 2018) and that 5 km is sufficient for the representation of katabatic storms (Oltmanns et al., 2014, 2015).

For ICON-O there has been no quantification of the effective resolution yet. With reference to the first baroclinic Rossby deformation radius calculated by LaCasce and Groeskamp (2020), which also takes bathymetry into account, we find a required resolution to resolve eddies of about  $1/25^\circ$  to  $1/12^\circ$  in the Irminger Sea (about 5 km to 2 km at  $60^\circ\text{N}$ ) and  $1/50^\circ$  (about 1 km) over the shelf.

ICON-A was run with the ECHAM6.3 physics (Giorgetta et al., 2018) and not with the Numerical Weather Prediction (NWP) physics. The reason is that the ECHAM6.3 physics is largely energy conserving, which is a necessity for studying coupled processes and climate. However, to account for the storm resolving resolution, several adjustments were made to the physical parameterizations in ICON-A. First, the atmospheric deep convection scheme was switched off. Further, parameterizations of subgrid-scale orographic effects (blocking and gravity wave drag) and non-orographic gravity wave drag were switched off and cloud microphysics were calculated using a three-category ice scheme, referred to as the graupel scheme. On the other hand, atmospheric subgrid-scale turbulence was parameterized with the 3D-Smagorinsky scheme, which has been implemented into ICON-A for large eddy simulation applications (Dipankar et al., 2015). In ICON-O, the mesoscale eddy parameterization (Gent-McWilliams (GM) closure) was switched off and vertical mixing was parameterized with the turbulent kinetic energy (TKE) closure (Gaspar et al., 1990; Blanke & Delecluse, 1993).

Before coupling, both components were spun up separately. The atmosphere was initialized from the global (9 km) European Centre for Medium Range Weather Forecasts (ECMWF) Integrated Forecasting System (IFS) analysis corresponding to 20 January 2020. Spinning up the ocean is more expensive. Therefore, the following strategy was used for this first 5 km coupled simulation. The initial fields were taken from PHC3.0 (Steele et al., 2001) and interpolated to a coarser 10 km grid. The ocean was spun up on this coarser grid using a combination of different atmospheric forcing data. First, 25 cycles were run with OMIP forcing, a climatology based on the ERA-40 years 1958–2001 (Simmons & Gibson, 2000), followed by NCEP (Kalnay et al., 1996) from 1948 to 2000 and ERA5 (Hersbach et al., 2020) from 2000 to 2010. Then, the ocean state was interpolated from the 10 km to the 5 km grid and the 10 recent years (2011 to 2020) were forced with ERA5 (Hersbach et al., 2020) to ensure the development of background features, such as ocean mesoscale eddies or currents. We note that the spin-up was produced with an older model version and was not repeated with the version of the production run due to computational costs.

Once coupled, atmospheric fluxes were exchanged every 15 minutes. The model was run for 21 simulation months, starting from 20 January 2020 and ending on 30 September 2021. However, we focus on the first winter and in particular on the 29 February when the katabatic storm develops. Before analyzing the fields, all output data has been interpolated by the nearest neighbour method onto a regular grid of  $0.05^\circ$ .

Using a global simulation has the advantage of avoiding arbitrary domain boundaries, such as in regional models, which would inevitably introduce artefacts that could influence the process under investigation (Leduc & Laprise, 2009; Giorgi, 2019). In ad-

237 dition, due to the global high resolution, the synoptic fields and the background state  
 238 of the ocean are expected to be more realistic than in comparable downscaling studies,  
 239 where only the nested simulation is run at high resolution, while the parent simulation  
 240 has a much coarser resolution. Furthermore, the small scales feed back to the large scales  
 241 and thereby modify the synoptics.

### 242 **3 Synoptic overview and katabatic storm development**

243 We analyze a katabatic storm appearing on the simulation day of 29 February 2020  
 244 and that has no real-time counterpart. This storm is the strongest of roughly 15 sim-  
 245 ilar events within the two simulation years, and its effect on the Irminger Sea is likely  
 246 most pronounced, which is why it was chosen for our case study. During the simulation,  
 247 no open ocean convection occurs in the Irminger Sea, and deeper mixed layers during  
 248 winter are only simulated along the western flank of the Reykjanes Ridge (600 to 900 m)  
 249 and along the EGIC (500 to 1300 m).

250 The storm develops when an upper-level trough crosses southeast Greenland. Within  
 251 the westerly flow, a lee trough forms east of Cape Farewell, Greenland’s southernmost  
 252 tip. Within the lee trough, the katabatic flow from the Ammassalik area triggers a pol-  
 253 ar low. The synoptic pressure gradient on the backside of the polar low amplifies the  
 254 katabatic winds in a positive feedback until the storm reaches near-surface wind speeds  
 255 of more than  $26 \text{ m s}^{-1}$  (Fig. 1) and almost  $50 \text{ m s}^{-1}$  in the low-level jet at the boundary  
 256 layer top.

257 On 28 February 2020 at 00 UTC, the centre of the upper-level trough is located over  
 258 western Greenland (Fig.2a). The southeast coast of Greenland is below the cyclonic side  
 259 of the diffluence zone of the jetstreak and hence an area favourable for upward motion  
 260 and cyclogenesis. Upper-level divergence and differential vorticity advection cause up-  
 261 ward motion diagnosed via the vorticity term in the  $\omega$ -equation. A LT forms east of Cape  
 262 Farewell (Fig.2a) and further preconditions the southeast coast of Greenland for cyclo-  
 263 genesis (Kristjánsson et al., 2011). These lee troughs form frequently east of Cape Farewell  
 264 in response to vortex stretching and potential vorticity (PV) conservation (Mc Innes et  
 265 al., 2009) when the westerly flow descends adiabatically from the high orography of Green-  
 266 land (Kristjánsson et al., 2011). A vertical transect along the Ikertivaq valley (Fig. 2b)  
 267 shows only weak winds near the surface and a stable stratification with cloud cover be-  
 268 low 2000 m.

269 Within the next 18 hours, the upper-level trough crosses southern Greenland and  
 270 its centre deepens to 496 gpdm over the Irminger Sea (Fig. 2c), showing a strong cyclonic  
 271 PV anomaly with more than 2 PVU at 500 hPa. At the surface, the pressure is falling  
 272 in response to the upper-level divergence that induces low-level convergence (Hoskins et  
 273 al., 1985; Bracegirdle & Gray, 2009). Katabatic flow is initiated by a superimposed pres-  
 274 sure gradient over the Ammassalik valleys and cold air is drained from the Greenland  
 275 ice sheet (Fig. 2d). Near the coast, the katabatic flow channels in the narrow valleys and  
 276 accelerates. This converging flow constitutes a low-level baroclinic instability and enhances  
 277 cyclonic vorticity due to vortex stretching, thereby increasing the PV anomaly (Klein  
 278 & Heinemann, 2002). As a measure for baroclinicity we calculate the maximum Eady  
 279 growth rate ( $\sigma_{max}$  in  $\text{s}^{-1}$ ) (Eady, 1949; Lindzen & Farrell, 1980; Dierer & Schlunzen,  
 280 2005) that describes how well deep pressure systems can develop in a weather situation  
 281 over a specific area, with positive values favouring cyclogenesis:

$$\sigma_{max} = 0.398 f \partial_z \mathbf{V}_h N^{-1}, \quad (1)$$

282 with  $f$  the Coriolis parameter,  $\partial_z \mathbf{V}_h$  the vertical wind shear, and  $N = \sqrt{g/\theta \partial_z \theta}$   
 283 the buoyancy frequency that depends on the gravitational constant  $g$  and the vertical

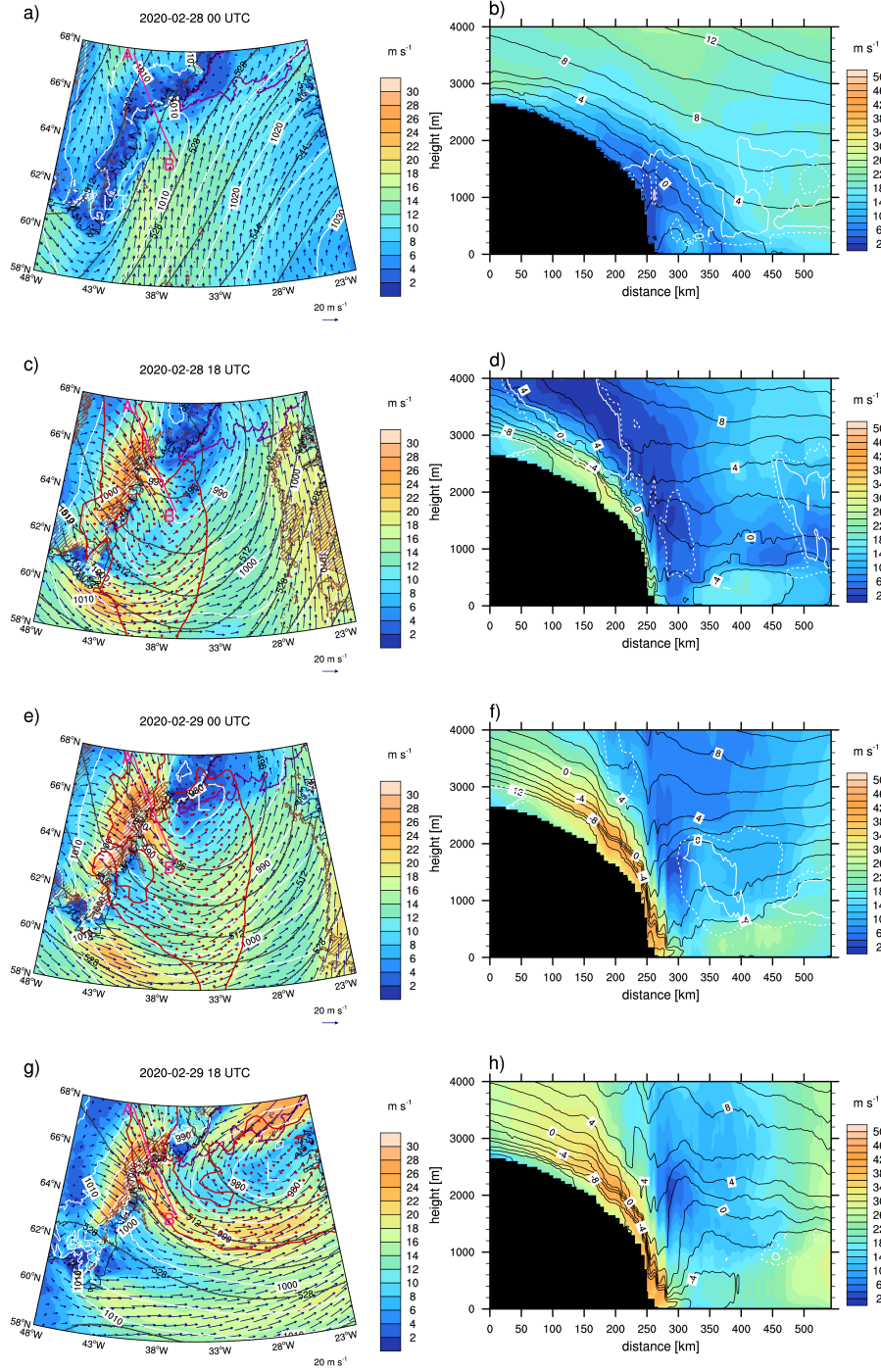


**Figure 2.** Development of the katabatic storm on 28 and 29 February 2020 in the Irminger Sea as simulated by ICON-ESM. The first column (a,c,e,g) shows the 10 m wind speed (6-hourly mean; colour shaded) and vectors, overlain by the mean-sea level pressure in hPa (white contours, every 5 hPa), the potential vorticity at 500 hPa ( $\geq 2$  PVU;  $1 \text{ PVU} = 10^{-6} \text{ K m}^2 \text{ kg}^{-1} \text{ s}^{-1}$ ; red contour and stippling), and the sea ice edge (15% ice concentration, purple contour). "LT" in a) marks the lee trough east of Cape Farewell, and "L" in e) and g) the position of the polar low. Brown hatching marks areas where the Eady growth rate averaged over the lowest 2000 m is larger than  $0.5 \cdot 10^{-4} \text{ s}^{-1}$ . The second column (b,d,f,h) shows the transects of wind speed (shaded colour), potential temperature in  $^{\circ}\text{C}$  (black contours) and cloud cover (25% as dashed white contours, 50% as solid white contours) through the Ikertivaq valley in the Ammassalik area (magenta line in first column).

284 gradient of the potential temperature  $\theta$ . The Ammassalik area is clearly a region of low-  
 285 level baroclinicity as indicated by the positive Eady growth rate in Fig. 2c.

286 Within the next 6 hours, the katabatic flow from Ammassalik triggers a polar low  
 287 with closed isobars on 29 February at 00 UTC and a core pressure of less than 980 hPa  
 288 (Fig. 2e). Converging flow, cold-air advection decreasing with height, and the baroclin-  
 289 icity in the Ammassalik area trigger the formation of the polar low (Klein & Heinemann,  
 290 2002) near the sea ice edge, where polar lows frequently form and intensify (Dierer &  
 291 Schluenzen, 2005; Bracegirdle & Gray, 2009). Furthermore, the coupling of the lower and  
 292 upper-level PV anomalies reinforces the polar low, which in turn deepens the upper-level  
 293 trough.

294 The Irminger Sea is known for polar low genesis and exhibits strong vertical tem-  
 295 perature differences (Kristjánsson et al., 2011). Although there is no universal definition  
 296 for a polar low (Kolstad, 2011), Blechschmidt et al. (2009) defined two criteria: 1) tem-  
 297 perature difference between the surface and at 500 hPa ( $SST - T_{500}$ ) of more than 48 K  
 298 and 2) an upper-level cyclonic PV anomaly. From 6-hourly averages, we find both cri-  
 299 teria roughly fulfilled with  $SST - T_{500} = 45$  K (not shown) and a positive PV anomaly  
 300 of more than 2 PVU at 500 hPa. Note that there are other thresholds used for the same  
 301 criterion, such as 43 K (Xia et al., 2012) or 40 K (Landgren et al., 2019), or other def-  
 302 initions, such as the MCAO index ( $SST - T_{700}$ ) (Kolstad et al., 2009). For our study,  
 303 the exact threshold or definition is not decisive.

304 On the back side of the polar low, the superimposed pressure gradient intensifies,  
 305 further accelerating the katabatic flow (Fig.2e) and draining increasingly cold air from  
 306 the Greenland ice sheet. The cold air spreads as a tongue over the Irminger Sea, where  
 307 it warms and causes atmospheric convection with cloud formation (Fig.2f). In addition,  
 308 a mountain or lee wave breaks at the steep slope of the topography (roughly at 250 km  
 309 distance) and transfers momentum downwards into the katabatic boundary layer (Oltmanns  
 310 et al., 2015) that further accelerates the katabatic flow. Once the polar low reaches ma-  
 311 ture state (Fig.2g,h), the wind speed peaks with hurricane intensity of almost  $50 \text{ m s}^{-1}$ .  
 312 The associated low-level jet is most intense near the top of the stable boundary layer.  
 313 Although the highest near-surface wind speeds occur over the shelf, the storm affects the  
 314 entire Irminger Sea, even reaching Iceland (Fig.2g).

315 These results suggest that four processes interact in the formation of the polar low  
 316 and cause this katabatic storm: 1) favourable conditions for cyclogenesis due to an upper-  
 317 level trough crossing South Greenland (upper-level divergence and positive vorticity ad-  
 318 vection or PV anomaly), 2) a lee trough east of Cape Farewell generating cyclonic vor-  
 319 ticity due to vortex stretching, 3) triggering of a polar low by katabatic flow due to baro-  
 320 clinicity of the converging flow from the Ammassalik valleys and a positive feedback with  
 321 the polar low that amplifies the katabatic flow, and 4) a breaking mountain wave that  
 322 transfers momentum downward into the surface boundary layer and causes additional  
 323 acceleration. Although we cannot generalize from this case study, it seems that all these  
 324 processes are of importance in the polar low formation in the Irminger Sea and for gen-  
 325 erating katabatic storms of hurricane intensity.

#### 326 **4 Air-sea interactions and water mass transformation over the shelf** 327 **and in the Irminger Sea**

328 The katabatic storm with its high wind speeds is expected to substantially mod-  
 329 ify the water of the southeast Greenland shelf, but also the western boundary current,  
 330 i.e. EGIC, and the upper ocean of the Irminger Basin, because the tongue of cold air and  
 331 high wind speeds extends across the entire basin and even reaches the western flank of  
 332 the Reykjanes Ridge (Fig. 2g).

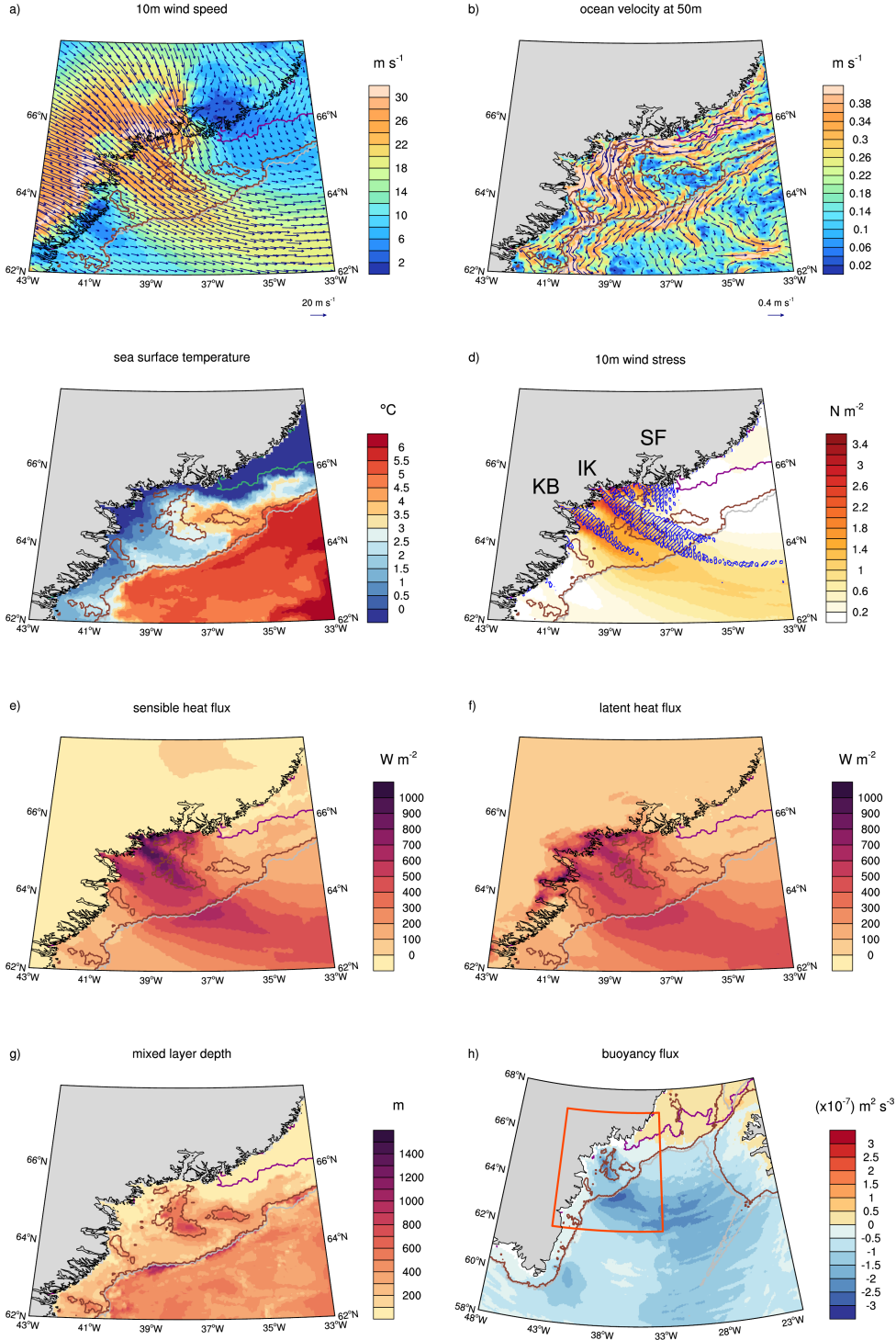


**Figure 3.** Air-sea interactions (daily means) in the Ammassalik area: a) 10 m wind speed (shaded colour) and vectors, b) ocean velocity at 50 m depth, c) sea surface temperature, d) 10 m wind stress and positive wind stress curl ( $\leq 0.15 \cdot 10^4 \text{ N m}^{-3}$  as blue hatching), e) sensible heat flux, f) latent heat flux, g) mixed layer depth ( $\sigma_t = 0.03 \text{ kg m}^{-3}$ ), and h) buoyancy flux. Overlain are the 500 m and 1000 m isobaths in m (brown and grey contours) and the 15% sea ice concentration (green in a) and c), magenta in all other). The fjord names in Ammassalik are indicated in d) with KG: Køge Bugt Fjord, IK: Ikertivaq, and SF: Sermilik Fjord. The orange box in h) marks the Ammassalik area for which the water mass transformation has been calculated.

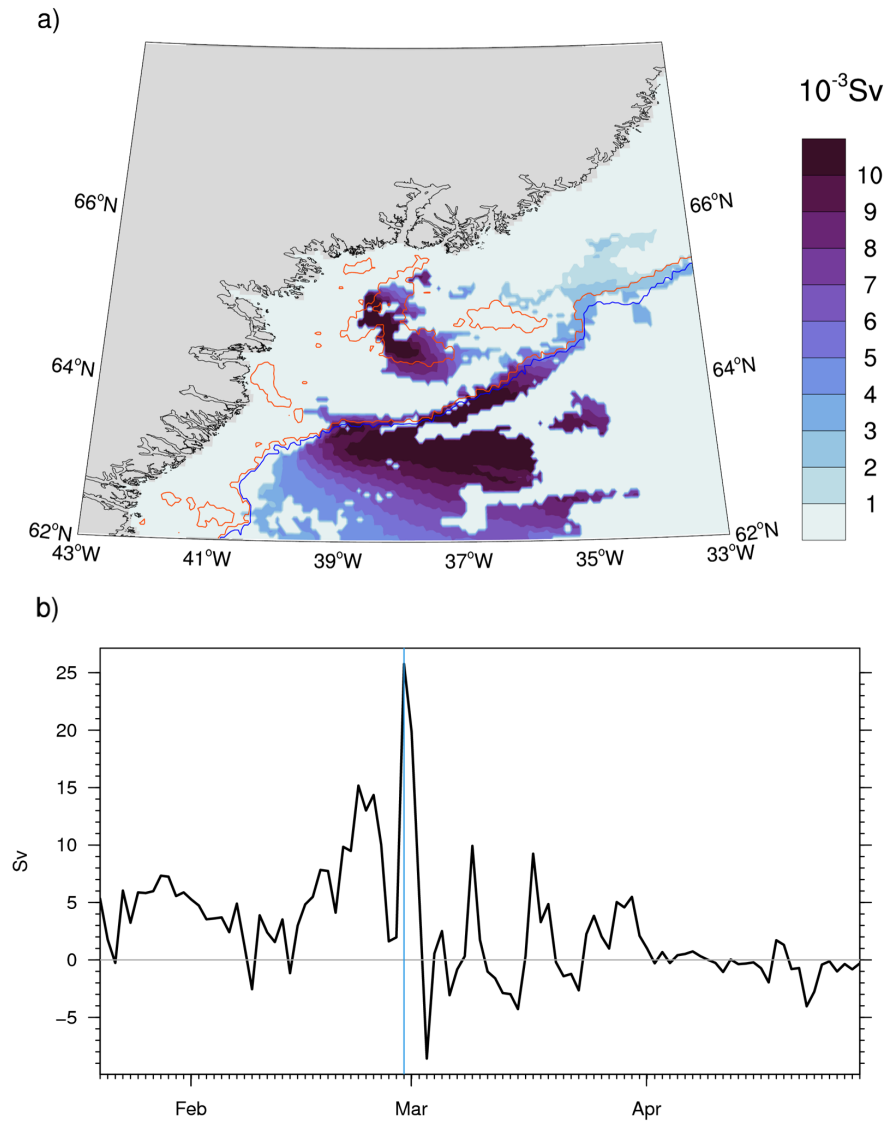


**Figure 4.** Water mass transformation (Sv) of density class  $\sigma = 27.6 \pm 0.025 \text{ kg m}^{-3}$  on a) 29 February 2020 during the katabatic storm. The coloured contours show the 500 m (orange) and 1000 m (blue) isobaths. b) time series of water mass transformation of same density class integrated over the area shown in a). The 29 February is marked by the vertical blue line.

333 The katabatic storm (daily means on 29 February 2020; Fig 3a) consists of two cones  
 334 of high wind speeds that merge over the southeast Greenland shelf, one from Ikertivaq  
 335 valley and the other from the K oge Bugt Fjord. We focus on the flow from the Ikerti-  
 336 vaq valley because it directly passes over the Sermilik Trough (ST), a bathymetric fea-  
 337 ture that reaches depths of about 800 m (An et al., 2019). The ST has recently received  
 338 attention because drifter data revealed that the East Greenland Current (EGC) steers  
 339 northwards on its northern flank, where it interacts with the East Greenland Coastal Cur-  
 340 rent (EGCC, Duyck & de Jong, 2021). Indeed, we find similar pathways of the EGC or  
 341 EGIC in our simulation (Fig. 3b) that agree well with trajectories of these drifters. The  
 342 main part of the EGIC flows along the shelf break, but a smaller fraction steers north-  
 343 ward into the ST with even a pathway that directly crosses the trough, as described by  
 344 Duyck and de Jong (2021).

345 The inflow of the relatively warm EGIC along the northern flank of the ST results  
 346 in warmer sea surface temperatures of about 3 to 4.5  C (Fig. 3c). These warmer SSTs  
 347 in the northern ST could be the reason why there is no sea ice present in the Ammas-  
 348 salik area. After mixing with the colder and fresher EGCC, but also because of substan-  
 349 tial heat loss to the atmosphere (Fig. 3e-f), the SSTs are colder (1.5 to 3  C) in the re-  
 350 turn flow in the southern ST. The sensible and latent heat fluxes reach daily mean val-  
 351 ues of 1000 W m<sup>-2</sup> over the ST during the event because of strong wind speeds and large  
 352 temperature and moisture contrasts. The high wind speeds exert strong wind stress (Fig. 3d)  
 353 on the upper ocean with positive wind stress curl over the ST that further contributes  
 354 to convection in the ST.

355 At the shelf break, the cold katabatic flow encounters the warmer waters of the re-  
 356 circulating Irminger Current and the turbulent heat fluxes peak for a second time with  
 357 values of about 700 W m<sup>-2</sup> for the sensible heat flux and 600 W m<sup>-2</sup> for the latent heat  
 358 flux. The sensible heat flux is higher during the event because the air-sea contrast is stronger  
 359 for temperature than for moisture.

360 The considerable heat loss from the ocean and momentum gain due to high wind  
 361 stress leads to convection and vertical mixing in the ST and on the shelf break, which  
 362 is visible as deep mixed layers ( $\sigma_t = 0.03 \text{ kg m}^{-3}$ ; Fig. 3h) in the ST and as a narrow band  
 363 along the shelf break. To quantify the effect of the katabatic storm on the ocean, we cal-  
 364 culated the buoyancy flux ( $B$ ) following Groeskamp et al. (2019), with a negative  $B$  mean-  
 365 ing buoyancy loss of the ocean:

$$B = \overline{w'b'} = \frac{g\alpha}{\rho_0 c_p} Q_0 + g\beta S(P - E), \quad (2)$$

366 with  $g$  the gravitational acceleration,  $\rho_0 = 1025.022 \text{ kg m}^{-3}$  the reference density,  
 367  $Q_0$  the net heat flux (in W m<sup>-2</sup>) at the ocean surface (positive into the ocean),  $\alpha$  and  
 368  $\beta$  the thermal expansion and haline contraction coefficients,  $S$  the salinity,  $P$  the pre-  
 369 cipitation (in ms<sup>-1</sup>) and  $E$  the evaporation (in ms<sup>-1</sup>). Note that we neglect the pen-  
 370 etration of shortwave radiation into the ocean, as it is anyway very small in winter. The  
 371 net heat flux at the ocean surface was calculated as:

$$Q_0 = Q_S + Q_L + Q_{SW} + Q_{LW}, \quad (3)$$

372 with  $Q_S$  the sensible heat flux,  $Q_L$  the latent heat flux,  $Q_{SW}$  the net shortwave  
 373 radiation and  $Q_{LW}$  the net longwave radiation.

374 The buoyancy loss is mainly determined by the turbulent heat fluxes. It peaks over  
 375 the ST and EGIC where the turbulent heat fluxes are largest, but there is also buoyancy  
 376 loss in the central Irminger Basin (Fig. 3g). Although there is no deep convection dur-  
 377 ing the simulated winter, these results suggest that katabatic storms can contribute to

378 precondition the Irminger Sea for deep convection. In contrast, a tip jet at Cape Farewell  
 379 occurring at the same day induces a buoyancy loss only near the coast. Even though we  
 380 analyze only a single event, the role of katabatic storms for triggering deep convection  
 381 could be underestimated simply because the atmospheric resolution has so far been too  
 382 coarse to resolve them. If true, katabatic winds could be of greater importance than has  
 383 been attributed to them so far Paquin et al. (2016).

384 We estimate the water mass transformation  $F(\sigma)$  ( $\text{m}^3 \text{s}^{-1}$ ) for density classes (or  
 385 bin size) enclosed by outcropping isopycnals of  $\Delta\sigma = 0.05 \text{ kg m}^{-3}$ , following the approach  
 386 of Petit et al. (2020) and Speer and Tziperman (1992). We calculate  $F(\sigma)$  from daily  
 387 mean values of the buoyancy flux:

$$F(\sigma) = \frac{1}{(g/\rho_0)\Delta\sigma} \iint -B \Pi(\sigma) dA, \quad (4)$$

where

$$\Pi(\sigma) = \begin{cases} 1, & \text{for } |\sigma - \sigma'| \leq \frac{\Delta\sigma}{2} \\ 0, & \text{otherwise} \end{cases} \quad (5)$$

388 with  $A$  the area enclosed by a density class.  $F(\sigma) > 0$  means that water is trans-  
 389 formed to this density class. We chose  $\Delta\sigma = 0.05 \text{ kg m}^{-3}$  and show the result for the  
 390 densest outcropping class of  $\sigma = 27.6 \pm \Delta\sigma/2 \text{ kg m}^{-3}$  during the katabatic storm on  
 391 29 February 2020 in Fig. 4a. Water mass transformation is largest in the ST and along  
 392 the EGIC, with an area downstream that also includes part of the inner basin (Fig. 4a).  
 393 Integrating over the area shown and considering the period from 20 January to 30 April  
 394 2020 shows that water mass transformation peaks during the katabatic storm. A day later,  
 395 on 1 March, the Ammassalik area is still influenced by the storm and water transforma-  
 396 tion remains high before dropping sharply after the storm subsides.

## 397 5 Vertical transects along the Ikertivaq valley and Sermilik Trough

398 Transects of daily mean quantities for 29 February 2020 along the Ikertivaq val-  
 399 ley and through the ST (Fig. 5) illustrate the air-sea interactions in the ST in more de-  
 400 tail.

401 On 29 February 2020 the superimposed strong pressure gradients associated with  
 402 the polar low cause velocities that reach almost  $50 \text{ m s}^{-1}$  over the steep slopes near the  
 403 coast and result in a tongue of high wind speeds reaching up to  $30 \text{ m s}^{-1}$  in the lower 1000 m  
 404 over the shelf (Fig. 5a). Where the slopes are steepest, there is a hydraulic jump and the  
 405 wind speed drops to very small values. This jump is associated with the breaking of a  
 406 mountain wave as described in Oltmanns et al. (2015). The mountain wave breaking trans-  
 407 fers momentum downwards, which can be seen by strong downward velocities (Fig. 5c)  
 408 that accelerate the katabatic flow (see details how this affects the dynamics of the katabatic  
 409 flow in Oltmanns et al. (2015)).

410 Over the ocean, the cold and dry air mass from the Greenland ice sheet (Fig. 5e)  
 411 encounter the relatively warm water of the ST (Fig. 5d). Convection with cloud forma-  
 412 tion is initiated in the atmosphere due to the unstable stratification (Fig. 5c). The clouds,  
 413 however, move quickly with the flow so that only a small fraction is visible in the daily  
 414 mean. The katabatic boundary layer is well visible from the potential temperature distri-  
 415 bution (Fig. 5e) and is about 200 to 400 m thick, which is typical for southeast Green-  
 416 land (Klein & Heinemann, 2002; Heinemann, 2003). As the cold and dry air mass warms  
 417 and moistens over the shelf, the stable boundary layer evolves into a convective bound-  
 418 ary layer, whose height increases with distance from the coast. The cold air outburst and  
 419 the subsequent convection and cloud formation could also further intensify the polar low.

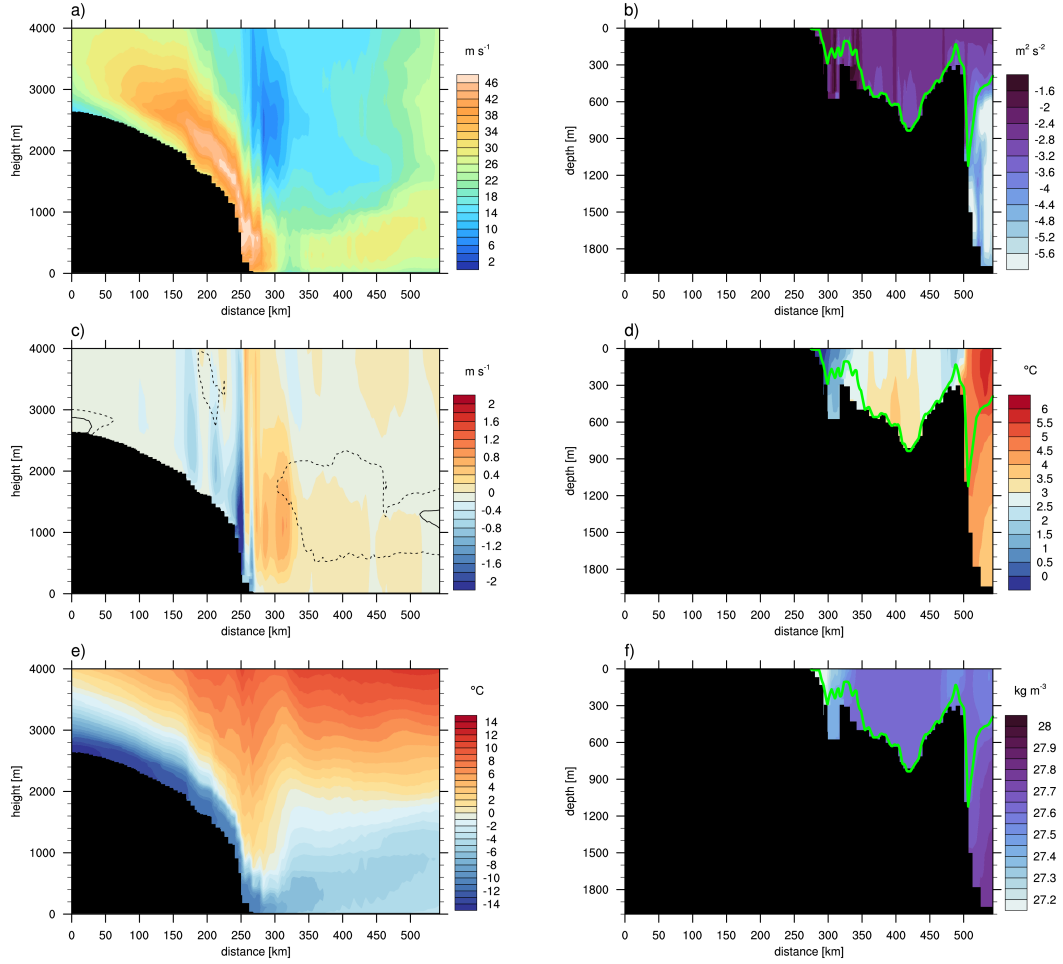


**Figure 5.** Vertical transects (daily means) along the Ikertivaq valley and Sermilik Trough: a) wind speed, b) turbulent kinetic energy in ocean, c) atmospheric vertical velocity with cloud cover (10% dashed and 50% solid contours), d) ocean potential temperature, e) atmospheric potential temperature, and f) ocean density ( $\sigma_{\Theta} = \sigma - 1000 \text{ kg m}^{-3}$ ). The green line in b), d), and f) marks the depth of the mixed layer ( $\sigma_{\Theta} = 0.03 \text{ kg m}^{-3}$ ).

420 The strong wind stress and heat fluxes cause intense vertical mixing and buoyancy  
 421 loss in the ST, resulting in large values of TKE (Fig.5b) reaching  $10^{-2} \text{ m}^2 \text{ s}^{-1}$  near the  
 422 surface. In fact, the entire water column in the ST is mixed, as can be seen from the mixed  
 423 layer reaching the bottom and the homogeneous density (Fig.5f) with the  $27.6 \text{ kg m}^{-3}$   
 424 isopycnal outcropping at the surface. However, the water mass is not homogeneous as  
 425 there is still structure in the temperature and salinity fields. The heat loss and the sub-  
 426 sequent cooling results in a mixed layer with densities of about  $\sigma_\theta = 27.6$  to  $27.65 \text{ kg m}^{-3}$ .  
 427 This density on the shelf and shelf break is close to the recently identified uSIW ( $\sigma_\theta =$   
 428  $27.65$  to  $27.73 \text{ kg m}^{-3}$ ) that forms at the edge of the western boundary (LeBras et al.,  
 429 2020).

430 The relatively warm temperatures of the EGIC induce a secondary peak of turbu-  
 431 lent heat flux and negative buoyancy flux at the shelf break, leading to densities in the  
 432 boundary current similar to those in the ST and a mixed layer depth of about 1100 m.  
 433 Dense water then leaves the ST and flows into the lower boundary current over the course  
 434 of the next couple of days (not shown). Both processes cause a densification of the bound-  
 435 ary current and thus contribute to the sinking of Atlantic water in the Irminger Sea. The  
 436 density anomalies are then transported downstream where they can even reach the Labrador  
 437 Sea.

## 438 6 Summary and conclusions

439 We have analyzed a mesoscale katabatic storm event of hurricane intensity over the  
 440 Irminger Sea and how it interacts with the ocean in the fully coupled, global climate model  
 441 ICON-ESM with storm-resolving (5 km) resolution. Katabatic storms have not been re-  
 442 solved hitherto in global models because of its small spatial extent, in particular in the  
 443 narrow valleys and fjords of Greenland. Our study is the first in which such an event and  
 444 its interactions with the ocean and feedback with the large-scale synoptics is simulated  
 445 in a global coupled climate model.

446 ICON-ESM is able to represent katabatic storms and other mesoscale wind systems  
 447 around Greenland with details previously described only by regional climate models. It  
 448 captures the complex interaction of the circulation with the steep orography of south-  
 449 east Greenland. A polar low forms within a lee trough environment over the Irminger  
 450 Sea that is initially triggered by the katabatic flow from the Ammassalik valleys. The  
 451 superimposed pressure gradient of the polar low accelerates the katabatic flow into a storm  
 452 but also deepens the upper-level trough. These results demonstrate the importance of  
 453 resolving the feedback of the small scales to the large scale in global climate models and  
 454 emphasizes the synoptic relevance of the Irminger Sea.

455 High resolution in the ocean allows resolving small-scale bathymetric features of  
 456 the southeast Greenland shelf, such as the Sermilik Trough, where the EGC interacts  
 457 with the EGCC and where water mass transformation takes place. Strong air-sea fluxes  
 458 caused by the katabatic storm induce substantial heat loss from the ocean and transfer  
 459 momentum to it. As a result, convection and mixing is induced in the Sermilik Trough  
 460 and along the shelf break, leading to density anomalies in the trough and boundary cur-  
 461 rent. Previous studies have shown that density anomalies in the boundary current of the  
 462 Irminger Sea caused by surface fluxes strongly influence AMOC variability.

463 The water mass formed within the Sermilik Trough and on the shelf during the katabatic  
 464 storm has a density that is close to the recently described upper Irminger Sea Inter-  
 465 mediate Water. Even though our simulation is rather short, we conclude that katabatic  
 466 storms are relevant for the densification of the western boundary current. Exper-  
 467 iments covering several decades with this class of models will be carried out in the Eu-  
 468 ropean Union "NextGEMs" project (<https://nextgems-h2020.eu>). These simulations  
 469 provide opportunities to explore further how dense water masses formed in the ST and

470 at the shelf edge together with denser water masses from deep convection and the over-  
 471 flows contribute to North Atlantic Deep water and its variability.

## 472 Open Research

473 Primary scripts to reproduce the figures and analyses can be obtained from MPG.PuRe  
 474 (<http://hdl.handle.net/21.11116/0000-0008-ECF1-E>, Gutjahr, Jungclaus, Brüggemann,  
 475 et al., 2021) and the model data from the WDC Long Term Archive ([http://cera-www](http://cera-www.dkrz.de/WDC/ui/Compact.jsp?acronym=DKRZ_LTA_033_ds00010)  
 476 [.dkrz.de/WDC/ui/Compact.jsp?acronym=DKRZ\\_LTA\\_033\\_ds00010](http://cera-www.dkrz.de/WDC/ui/Compact.jsp?acronym=DKRZ_LTA_033_ds00010), Gutjahr, Jungclaus,  
 477 Brüggemann, et al., 2021). The model code of ICON is available to individuals under  
 478 licenses (<https://mpimet.mpg.de/en/science/modeling-with-icon/code-availability>).  
 479 The buoyancy fluxes and the water mass transformation were calculated with R 4.0.2  
 480 (R Core Team, 2020) and the oce package version 1.3-0 (Kelley & Richards, 2021).

## 481 Acknowledgments

482 This work is a contribution to the project S2 (Improved Parameterizations and Numerics  
 483 in Climate Models) of the Collaborative Research Centre TRR 181 "Energy Transfer  
 484 in Atmosphere and Ocean" funded by the Deutsche Forschungsgemeinschaft (DFG,  
 485 German Research Foundation) - project number 274762653 and the Max Planck Soci-  
 486 ety for the Advancement of Science. The research was supported by the European Union  
 487 Horizon 2020 collaborative project NextGEMS (grant number 101003470). DYAMOND  
 488 data management was provided by the Deutsches Klimarechenzentrum (DKRZ) and sup-  
 489 ported through the projects ESiWACE and ESiWACE2. The projects ESiWACE and  
 490 ESiWACE2 have received funding from the European Union's Horizon 2020 research and  
 491 innovation program under grant agreements No 675191 and 823988. This work used re-  
 492 sources of the Deutsches Klimarechenzentrum (DKRZ) granted by its Scientific Steer-  
 493 ing Committee (WLA) under project IDs bk1040 and bb1153. We thank the DYAMOND  
 494 Winter (<https://www.esiwace.eu/services/dyiamond/winter>) team at MPI-M and  
 495 DKRZ for producing the simulation. We further thank Elisa Manzini for providing con-  
 496 structive comments.

## 497 References

- 498 An, L., Rignot, E., Chauche, N., Holland, D., Holland, D., Jakobsson, M., . . . Willis,  
 499 J. K. (2019). Bathymetry of southeast Greenland from oceans melting Green-  
 500 land (OMG) data. *Geophysical Research Letters*, *46*, 11197–11205. doi:  
 501 10.1029/2019GL083953
- 502 Bacon, S., Gould, W. J., & Jia, Y. L. (2003). Open-ocean convection in the Irminger  
 503 Sea. *Geophys. Res. Lett.*, *30*, 1246. doi: 10.1029/2002GL016271
- 504 Blanke, B., & Delecluse, P. (1993). Variability of the Tropical Atlantic Ocean Simu-  
 505 lated by a General Circulation Model with Two Different Mixed-Layer Physics.  
 506 *J. Phys. Oceanogr.*, *23*(7), 1363–1388. doi: 10.1175/1520-0485(1993)023<1363:  
 507 VOTTAO>2.0.CO;2
- 508 Blechschmidt, A.-M., Bakan, S., & Graßl, H. (2009). Large-scale atmospheric cir-  
 509 culation patterns during polar low events over the Nordic seas. *J. Geophys.*  
 510 *Res.*(D06115). doi: 10.1029/2008JD010865
- 511 Bracegirdle, T. J., & Gray, S. L. (2008). An objective climatology of the dynamical  
 512 forcing of polar lows in the Nordic Seas. *Int. J. Climatol.*, *28*, 1903–1919. doi:  
 513 10.1002/joc.1686
- 514 Bracegirdle, T. J., & Gray, S. L. (2009). The dynamics of a polar low assessed using  
 515 potential vorticity inversion. *Quarterly Journal of the Royal Meteorological So-*  
 516 *ciety*, *135*, 880–893. doi: 10.1002/qj.411
- 517 Chafik, L., & Rossby, T. (2019). Volume, Heat, and Freshwater Divergences in  
 518 the Subpolar North Atlantic Suggest the Nordic Seas as Key to the State of

- 519 the Meridional Overturning Circulation. *Geophysical Research Letters*, *46*,  
520 4799–4808. doi: 10.1029/2019GL082110
- 521 Condron, A., Bigg, G. R., & Renfrew, I. A. (2008). Modeling the impact of polar  
522 mesocyclones on ocean circulation. *J. Geophys. Res.*, *113*(C10005). doi: 10  
523 .1029/2007JC004599
- 524 de Jong, M. F., Oltmanns, M., Karstensen, J., & de Steur, L. (2018). Deep Convec-  
525 tion in the Irminger Sea Observed with a Dense Mooring Array. *Oceanography*,  
526 *31*, 50–59. doi: 10.5670/oceanog.2018.109
- 527 de Jong, M. F., van Aken, H. M., Våge, K., & Pickart, R. S. (2012). Convective mix-  
528 ing in the central Irminger Sea: 2002–2010. *Deep-Sea Res. I*, *63*, 36–51. doi:  
529 10.1016/j.dsr.2012.01.003
- 530 Desbruyères, D., Mercier, H., Maze, G., & Daniault, N. (2019). Surface predic-  
531 tor of overturning circulation and heat content change in the subpolar North  
532 Atlantic. *Ocean Sci.* doi: 10.5194/os-15-809-2019
- 533 Dierer, S., & Schlunzen, K. H. (2005). Influence parameters for a polar mesocy-  
534 clone development. *Meteorologische Zeitschrift*, *14*, 781–792. doi: 10.1127/0941  
535 -2948/2005/0077
- 536 Dipankar, A., Stevens, B., Heinze, R., Moseley, C., Zängl, G., Giorgetta, M., & Br-  
537 dar, S. (2015). Large eddy simulation using the general circulation model  
538 ICON. *J. Adv. Model. Earth Syst.*, *7*, 963–986. doi: 10.1002/2015MS000431
- 539 DuVivier, A. K., & Cassano, J. J. (2013). Evaluation of WRF Model Resolution on  
540 Simulated Mesoscale Winds and Surface Fluxes near Greenland. *Mon. Weather*  
541 *Rev.*, *141*(3), 941–963. doi: 10.1175/MWR-D-12-00091.1
- 542 Duyck, E., & de Jong, M. F. (2021). Circulation over the South-East Greenland  
543 Shelf and Potential Freshwater Export: a Drifter Study. *Geophysical Research*  
544 *Letters*, *48*, e2020GL091948. doi: 10.1029/2020GL091948
- 545 Eady, E. (1949). Long waves and cyclone waves. *Tellus*, *1*, 33–52. doi: 10.1111/  
546 j.2153-3490.1949.tb01265.x
- 547 Eyring, V., Bony, S., Meehl, G. A., Senior, C. A., Stevens, B., Stouffer, R. J., &  
548 Taylor, K. E. (2016). Overview of the Coupled Model Intercomparison Project  
549 Phase 6 (CMIP6) experimental design and organization. *Geosci. Model Dev.*,  
550 *9*, 1937–1958. doi: 10.5194/gmd-9-1937-2016
- 551 Gaspar, P., Grégoris, Y., & Lefevre, J.-M. (1990). A simple eddy kinetic energy  
552 model for simulations of the oceanic vertical mixing: Tests at station Papa  
553 and long-term upper ocean study site. *J. Geophys. Res. Oceans*, *95*(C9),  
554 16179–16193. doi: 10.1029/JC095iC09p16179
- 555 Giorgetta, M. A., Brokopf, R., Crueger, T., Esch, M., Fiedler, S., Helmert, J., ...  
556 Stevens, B. (2018). ICON-A, the Atmosphere Component of the ICON Earth  
557 System Model: I. Model Description. *Journal of Advances in Modeling Earth*  
558 *Systems*, *10*, 1613–1637. doi: 10.1029/2017MS001242
- 559 Giorgi, F. (2019). Thirty years of regional climate modelling: where are we and  
560 where are we going next? *Journal of Geophysical Research: Atmospheres*, *124*,  
561 5696–5723. doi: 10.1029/2018JD030094
- 562 Groeskamp, S., Griffies, S. M., Iudicone, D., Marsh, R., Nurser, A. J. G., & Zika,  
563 J. D. (2019). The Water Mass Transformation Framework for Ocean Physics  
564 and Biogeochemistry. *Annual Review of Marine Science*, *11*, 271–305. doi:  
565 10.1146/annurev-marine-010318-095421
- 566 Gutjahr, O., & Heinemann, G. (2018). A model-based comparison of extreme winds  
567 in the Arctic and around Greenland. *Int. J. Climatol.*, *38*, 5272–5292. doi: 10  
568 .1002/joc.5729
- 569 Gutjahr, O., Jungclaus, J. H., Brüggemann, N., Haak, H., & Marotzke, J. (2021).  
570 *Air-sea interactions and water mass transformation during a katabatic storm*  
571 *in the Irminger Sea – Scripts*. Retrieved from [http://hdl.handle.net/  
572 21.11116/0000-0008-ECF1-E](http://hdl.handle.net/21.11116/0000-0008-ECF1-E) (last access: 07.10.2021)
- 573 Gutjahr, O., Jungclaus, J. H., Brüggemann, N., Haak, H., & Marotzke, J. (2021).

- 574 *Air-sea interactions during a katabatic storm in the Irminger Sea simulated*  
575 *by a globally coupled storm-resolving (5 km) climate model - ICON Dyamond*  
576 *Winter simulation data.* World Data Center for Climate (WDCC) at DKRZ.  
577 Retrieved from [http://cera-www.dkrz.de/WDCC/ui/Compact.jsp?acronym=](http://cera-www.dkrz.de/WDCC/ui/Compact.jsp?acronym=DKRZ\LTA\_033\_ds00010)  
578 [DKRZ\LTA\\\_033\\\_ds00010](http://cera-www.dkrz.de/WDCC/ui/Compact.jsp?acronym=DKRZ\LTA\_033\_ds00010) (last access: 03.08.2021)
- 579 Haarsma, R. J., Roberts, M. J., Vidale, P. L., Senior, C. A., Bellucci, A., Bao, Q.,  
580 ... von Storch, J.-S. (2016). High Resolution Model Intercomparison Project  
581 (HighResMIP v1.0) for CMIP6. *Geosci. Model Dev.*, 9(11), 4185–4208. doi:  
582 10.5194/gmd-9-4185-2016
- 583 Heinemann, G. (2003). Forcing and feedback mechanisms between the katabatic  
584 wind and sea ice in the coastal areas of polar ice sheets. *The Global Atmo-*  
585 *sphere and Ocean System*, 9(4), 169–201. doi: 10.1080/1023673042000198130
- 586 Heinemann, G., & Klein, T. (2002). Modelling and observations of the katabatic  
587 flow dynamics over Greenland. *Tellus A: Dynamic Meteorology and Oceanogra-*  
588 *phy*, 54(5), 542–554. doi: 10.3202/tellusa.v54i5.12167
- 589 Hersbach, H., Bell, B., Berrisford, P., Hirahara, S., Horányi, A., Muñoz-Sabater,  
590 J., ... Thépaut, J.-N. (2020). The ERA5 global reanalysis. *Quarterly*  
591 *Journal of the Royal Meteorological Society*, 146(730), 1999–2049. doi:  
592 <https://doi.org/10.1002/qj.3803>
- 593 Hoskins, B. J., McIntyre, M. E., & Robertson, A. W. (1985). On the use and signif-  
594 icance of isentropic potential vorticity maps. *Q. J. R. Meteorol.*, 111, 877–946.  
595 doi: 10.1002/qj.49711147002
- 596 Jungclaus, J., Lorenz, S. J., Schmidt, H., Brovkin, V., Brüggemann, N., Chegini, F.,  
597 ... Claussen, M. (2021). The ICON Earth System Model Version 1.0. *Earth*  
598 *and Space Science Open Archive*, 44. doi: 10.1002/essoar.10507989.1
- 599 Kalnay, E., Kanamitsu, M., Kistler, R., Collins, W., Deaven, D., Gandin, L., ...  
600 Joseph, D. (1996). The ncep/ncar 40-year reanalysis project. *Bulletin*  
601 *of the American Meteorological Society*, 77(3), 437 - 472. Retrieved from  
602 [https://journals.ametsoc.org/view/journals/bams/77/3/1520-0477](https://journals.ametsoc.org/view/journals/bams/77/3/1520-0477_1996_077_0437_tnyrnp_2.0_co_2.xml)  
603 [\\_1996\\_077\\_0437\\_tnyrnp\\_2.0\\_co\\_2.xml](https://journals.ametsoc.org/view/journals/bams/77/3/1520-0477_1996_077_0437_tnyrnp_2.0_co_2.xml) doi: 10.1175/1520-0477(1996)077<0437:  
604 TNYRNP>2.0.CO;2
- 605 Kelley, D., & Richards, C. (2021). `oce`: Analysis of oceanographic data [Com-  
606 puter software manual]. Retrieved from [https://CRAN.R-project.org/](https://CRAN.R-project.org/package=oce)  
607 [package=oce](https://CRAN.R-project.org/package=oce) (R package version 1.3-0)
- 608 Klaver, R., Haarsma, R., Vidale, P. L., & Hazeleger, W. (2020). Effective reso-  
609 lution in high resolution global atmospheric models for climate studies. *Atmos*  
610 *Sci Lett.*, 21, e952. doi: 10.1002/asl.952
- 611 Klein, T., & Heinemann, G. (2002). Interaction of katabatic winds and mesocy-  
612 clones near the eastern coast of Greenland. *Meteorol. Appl.*, 9, 407–422. doi:  
613 10.1017/S1350482702004036
- 614 Kolstad, E. W. (2011). A global climatology of favourable conditions for polar lows.  
615 *Quarterly Journal of the Meteorological Society*, 137, 1749–1761. doi: 10.1002/  
616 qj.888
- 617 Kolstad, E. W., Bracegirdle, T. J., & Seierstad, I. A. (2009). Marine cold-air  
618 outbreaks in the North Atlantic: temporal distribution and associations  
619 with large-scale atmospheric circulation. *Clim. Dynam.*, 33, 187–197. doi:  
620 10.1007/s00382-008-0431-5
- 621 Korn, P. (2017). Formulation of an unstructured grid model for global ocean dynam-  
622 ics. *J. Comp. Physiol.*, 339, 525–552. doi: 10.1016/j.jcp.2017.03.009
- 623 Kristjánsson, J. E., Thorsteinsson, S., Kolstad, E. W., & Blechschmidt, A.-M.  
624 (2011). Orographic influence of east Greenland on a polar low over the Den-  
625 mark Strait. *Quarterly Journal of the Meteorological Society*, 137, 1773–1789.  
626 doi: 10.1002/qj.831
- 627 LaCasce, J. H., & Groeskamp, S. (2020). Baroclinic Modes over Rough Bathymetry  
628 and the Surface Deformation Radius. *J. Phys. Oceanogr.*, 50, 2835–2847. doi:

- 629 10.1175/JPO-D-20-0055.1
- 630 Landgren, O. A., Batrak, Y., Haugen, J. E., Støylen, E., & Iversen, T. (2019). Polar  
631 low variability and future projections for the Nordic and Barents Seas. *Quar-*  
632 *terly Journal of the Royal Meteorological Society*, *145*(724), 3116–3128. Re-  
633 trieved from [https://rmets.onlinelibrary.wiley.com/doi/abs/10.1002/](https://rmets.onlinelibrary.wiley.com/doi/abs/10.1002/qj.3608)  
634 [qj.3608](https://doi.org/10.1002/qj.3608) doi: <https://doi.org/10.1002/qj.3608>
- 635 LeBras, I. A.-A., Straneo, F., Holte, J., de Jong, M. F., & Holliday, N. P. (2020).  
636 Rapid export of waters formed by convection near the Irminger Sea’s west-  
637 ern boundary. *Geophysical Research Letters*, *47*(e2019GL085989). doi:  
638 10.1029/2019GL059898
- 639 Leduc, M., & Laprise, R. (2009). Regional climate model sensitivity to domain size.  
640 *Climate Dynamics*, *32*, 833–854. doi: 10.1007/s00382-008-0400-z
- 641 Lindzen, R., & Farrell, B. (1980). A simple approximate result for the maximum  
642 growth rate of baroclinic instabilities. *Journal of the Atmospheric Sciences*,  
643 *37*, 1648–1654.
- 644 Lozier, M. S., Li, F., Bacon, S., Bahr, F., Bower, A. S., Cunningham, S. A., ...  
645 Zhao, J. (2019). A sea change in our view of overturning in the subpolar North  
646 Atlantic. *Science*, *363*(6426), 516–521. doi: 10.1126/science.aau6592
- 647 Mc Innes, H., Kristiansen, J., Kristjánsson, J. E., & Schyberg, H. (2011). The role  
648 of horizontal resolution for polar low simulations. *Q. J. R. Meteorol. Soc.*,  
649 *137*(660), 1674–1687. doi: 10.1002/qj.849
- 650 Mc Innes, H., Kristjánsson, J. E., Schyberg, H., & Røsting, B. (2009). An assess-  
651 ment of a Greenland lee cyclone during the Greenland Flow Distortion exper-  
652 iment: An observational approach. *Quarterly Journal of the Meteorological*  
653 *Society*, *135*, 1968–1985. doi: 10.1102/qj.524
- 654 Menary, M. B., Jackson, L., & Lozier, M. S. (2020). Reconciling the Relation-  
655 ship Between the AMOC and Labrador Sea in OSNAP Observations and  
656 Climate Models. *Geophysical Research Letters*, *47*, e2020GL089793. doi:  
657 10.1029/2020GL089793
- 658 Moreno-Ibáñez, M., Laprise, R., & Gachon, P. (2021). Recent advances in polar  
659 low research: current knowledge, challenges and future perspectives. *Tellus A:*  
660 *Dynamic Meteorology and Oceanography*, *73*(1), 1–31. doi: 10.1080/16000870  
661 .2021.1890412
- 662 Neumann, P., Düben, P., Adamidis, P., Bauer, P., Brück, M., Kornbluh, L., ...  
663 Biercamp, J. (2019). Assessing the scales in numerical weather and cli-  
664 mate predictions: will exascale be the rescue? *Phil. Trans. R. Soc. A*, *377*,  
665 20180148. doi: 10.1098/rsta.2018.0148
- 666 Oltmanns, M., Straneo, F., Moore, G. W. K., & Mernild, S. H. (2014). Strong  
667 downslope wind events in Ammassalik, southeast Greenland. *J. Climate*, *27*,  
668 977–993. doi: 10.1175/jcli-d-13-00067.1
- 669 Oltmanns, M., Straneo, F., Seo, H., & Moore, G. W. K. (2015). Role of Wave  
670 Dynamics and Small-Scale Topography for Downslope Wind Events in South-  
671 east Greenland. *Journal of the Atmospheric Sciences*, *72*, 2786–2805. doi:  
672 10.1175/JAS-D-14-0257.1
- 673 Paquin, J.-P., Lu, Y., Higginson, S., Dupont, F., & Garric, G. (2016). Modelled  
674 variability of deep convection in the Irminger Sea during 2003–10. *J. Phys.*  
675 *Oceanogr.*, *46*, 179–196. doi: 10.1175/JPO-D-15-0078.1
- 676 Petit, T., Lozier, M. S., Josey, S. A., & Cunningham, S. A. (2020). Atlantic Deep  
677 Water Formation Occurs Primarily in the Iceland Basin and Irminger Sea by  
678 Local Buoyancy Forcing. *Geophys. Res. Lett.*, *47*, e2020GL091028. doi:  
679 10.1029/2020GL091028
- 680 Pickart, R. S., Spall, M. A., Ribergaard, M. H., Moore, G. W. K., & Milliff, R. F.  
681 (2003). Deep convection in the Irminger Sea forced by the Greenland tip jet.  
682 *Nature*, *424*(6945), 152–156. doi: 10.1038/nature01729
- 683 R Core Team. (2020). R: A language and environment for statistical computing

- 684 [Computer software manual]. Vienna, Austria. Retrieved from <https://www.R>  
685 [-project.org/](https://www.R-project.org/)
- 686 Rasmussen, L. (1989). Greenland winds and satellite imagery. *Vejret-Danish Meteor.*  
687 *Soc.*, 32–37.
- 688 Rühls, S., Oliver, E. C. J., Biastoch, A., Böning, C. W., Dowd, M., Getzlaff, K., ...  
689 Myers, P. G. (2021). Changing Spatial Patterns of Deep Convection in the  
690 Subpolar North Atlantic. *Journal of Geophysical Research: Oceans*, 126(7),  
691 e2021JC017245. doi: <https://doi.org/10.1029/2021JC017245>
- 692 Simmons, A., & Gibson, J. (2000, 03). The era-40 project plan. (1), 62. Retrieved  
693 from <https://www.ecmwf.int/node/12272>
- 694 Skamarock, W. C. (2004). Evaluating Mesoscale NWP Models Using Kinetic Energy  
695 Spectra. *Mon. Weather Rev.*, 132(12), 3019–3032. doi: 10.1175/MWR2830.1
- 696 Speer, K., & Tziperman, E. (1992). Rates of water mass formation in the North At-  
697 lantic ocean. *J. Phys. Oceanogr.*, 22, 93–104. doi: 10.1175/1520-0485(1992)  
698 022(0093:ROWMFI)2.0.CO;2
- 699 Steele, M., Morley, R., & Ermold, W. (2001). PHC: A global ocean hydrography  
700 with a high quality Arctic Ocean. *J. Climate*, 14, 2079–2087.
- 701 Stevens, B., Satoh, M., Auger, L., Biercamp, J., Bretherton, C., Chen, X., ... Zhou,  
702 L. (2019). DYAMOND: The DYnamics of the Atmospheric circulation Mod-  
703 eled On Non-hydrostatic Domains. *Progress in Earth and Planetary Science*,  
704 6(61). doi: 10.1186/s40645-019-0304-z
- 705 Stoll, P. J., Graverson, R. G., Noer, G., & Hodges, K. (2018). An objec-  
706 tive global climatology of polar lows based on reanalysis data. *Quarterly*  
707 *Journal of the Royal Meteorological Society*, 144(716), 2099–2117. doi:  
708 <https://doi.org/10.1002/qj.3309>
- 709 Xia, L., Zahn, M., Hodges, K. I., Feser, F., & von Storch, H. (2012). A compar-  
710 ison of two identification and tracking methods for polar lows. *Tellus A: Dy-*  
711 *namic Meteorology and Oceanography*, 64(1), 17196. doi: 10.3402/tellusa.v64i0  
712 .17196
- 713 Yeager, S., Castruccio, F., Chang, P., Danabasoglu, G., Maroon, E., Small, J., ...  
714 Zhang, S. (2021). An outsized role for the Labrador Sea in the multidecadal  
715 variability of the Atlantic overturning circulation. *Science Advances*, 7(41),  
716 eabh3592. doi: 10.1126/sciadv.abh3592
- 717 Zahn, M., & von Storch, H. (2008). A long-term climatology of North Atlantic polar  
718 lows. *Geophys. Res. Lett.*, 35, L22702. doi: 10.1029/2008GL035769
- 719 Zängl, G., Reinert, D., Rípodas, P., & Baldauf, M. (2015). The ICON (ICOsahedral  
720 Non-hydrostatic) modelling framework of DWD and MPI-M: Description of  
721 the non-hydrostatic dynamical core. *Quarterly Journal of the Royal Meteorolo-*  
722 *gical Society*, 141, 563–579. doi: 10.1002/qj.2378